Contents list available at CBIORE journal website

International Journal of Renewable Energy Development

Journal homepage: https://ijred.cbiore.id

Research Article

A double-Gaussian wake model considering yaw misalignment

Qidun Maulana Binu Soesanto[a*], Qidir Maulana Binu Soesanto[b], Puji Widiyanto[a]

[a]*Research Center for Energy Conversion and Conservation (PRKKE), Research Organization for Energy and Manufacture (OREM), National Research and Innovation Agency (BRIN), Indonesia*

[b]*Department of Physics, Faculty of Science and Mathematics (MIPA), Diponegoro University (UNDIP), Indonesia*

Abstract. A wake steering has been known to effectively increase wind farm production by deflecting the upstream turbines' wakes via yaw misalignment, thus minimizing their negative impacts on the downstream turbines' performances. This study presents analytical modeling of horizontal-axis wind turbine (HAWT) wake using low-cost analytical modeling as an alternative to expensive numerical and experimental trials. The existing double-Gaussian (DG) analytical wake model was modified to include the yaw misalignment effect, allowing its usability for the yawed HAWT wake modeling. The benchmark dataset produced by high-fidelity large eddy simulation (LES) of wake flowfields behind the turbine with yaw angles of 0°, 10°, 20°, and 30° were used to validate the accuracy of the DG yaw wake model. Overall, the DG yaw wake model predictions showed good agreement with the benchmark dataset under varying HAWT rotor yaw configurations. The analytical results verified by the LES dataset confirm the effectiveness of yaw misalignment in deflecting the wake trajectory, expediting the wake recovery downstream of the HAWT. In addition, a higher rotor yaw angle improves the wake recovery rate in the prevailing wind direction. Notable deviations against the benchmark dataset were found mainly within the near-wake region owing to flow acceleration arising from turbine-induced turbulence. As a result, the model's predictions were slightly lower than the benchmark dataset, most likely due to neglecting the acceleration term in the analytical model derivation. Otherwise, the analytical model could accurately predict the mean wake velocity within the far-wake region for all evaluated cases, demonstrating its reliability in estimating wind speed potential within a practical distance for micrositing. These results were also proved quantitatively by statistical evaluations utilizing root mean square error (RMSE) and Pearson correlation coefficient *R*. The present study points out the importance of the upstream HAWTs' rotor yaw controls to properly deflect their wakes away from their mainstream trajectories, thus effectively maximizing the wind speed potentials extracted by the downstream HAWTs and improving the overall wind farm production.

Keywords: Horizontal-axis wind turbine, yaw misalignment, yaw angle, wake deflection, double-Gaussian yaw wake model

Received: 30th Sep 2024; Revised: 7th Nov 2024; Accepted: 10th Dec 2024; Available online: 30th Dec 2024

1. Introduction

In the electricity generation sector, an enormous amount of wind energy potential has been attention among policymakers and researchers to place it as a main contributor to net-zero emissions. In general, its potential can be harvested from onshore and offshore terrains. For multi-megawatt projects, an offshore wind condition shows its viability owing to its stable and fast wind speed without micrositing constraints and relatively far from residents. Over the past decade, a rapid advancement in technological development of the offshore wind turbine has brought a new achievement for constructing a giant 16 MW horizontal-axis wind turbine (HAWT) with a rotor diameter of 242 meters (Evwind, 2021).

It is common to harvest wind's kinetic energy using a wind power plant or a wind farm, by clustering HAWTs under certain layout configurations to optimally extract the wind resources. However, some issues were reported, mainly related to wake effects that caused 40% power loss and increased fatigue loads by approximately 80% (Wang *et al.*, 2023). The wake itself is simply described as a plume-like region that evolves downstream of the turbine, characterized by velocity reduction and increased turbulence intensity (Archer *et al.*, 2018). The wake effects are strongly attributed to atmospheric stratification (Abkar & Porté-Agel, 2015) and turbine layout configuration (McTavish *et al.*, 2013; Meyers & Meneveau, 2012). In addition, the added turbulence intensity generated by the turbine also contributes to the wake recovery rate (Cheng & Porté-Agel, 2018), thus having a direct influence on the downstream turbine output.

Given the importance of wake losses on the overall wind farm performance, scientific investigations have been conducted to elucidate the wake behavior. An experimental investigation was undertaken to highlight the benefit of a lab-scale wind farm arranged into closely spaced lateral wind turbine configurations in the atmospheric boundary layer wind tunnel (McTavish *et al.*, 2013). It was found that those configurations have the potential to increase the annual capacity factor of a wind farm and reduce the land use requirements. However, since the Reynolds numbers in the model-scale turbines were smaller than those of utility-scale turbines (Pinto *et al.*, 2020; Yu-Ting *et al.*, 2019), thus some essential

* Corresponding author
Email: qidu001@brin.go.id (Q. M. B. Soesanto)

https://doi.org/10.61435/ijred.2025.60690
ISSN: 2252-4940/© 20xx.The Author(s). Published by CBIORE

characteristics, such as the length of the far-wake onset, could be different (Soesanto *et al*., 2022).

As an alternative to experimental trials, numerical simulation based on computational fluid dynamics (CFD) can be employed. In CFD, the large eddy simulation (LES) approach, which models the unsteady behavior of large-scale turbulent eddies, was often used to simulate the wake flowfields and their interference impacts on the wind farm performances (Archer *et al*., 2013; Creech *et al*., 2015; Ghaisas *et al*., 2017; Porté-Agel *et al*., 2013; Wu *et al*., 2020). The LES was also used to simulate fully developed flow within a wind farm under an atmospheric boundary layer (ABL), where the turbines were modeled using the classic drag disk concept at various turbine configurations, loading factors, and surface roughness (Calaf *et al*., 2010). The results were used to quantify the vertical transport of momentum and kinetic energy across the boundary layer.

Furthermore, the LES was also employed to predict the aerodynamics and power production of the Lillgrund offshore wind farm containing 48 megawatt-scale wind turbines using an in-house solver based on the OpenFOAM CFD toolbox (Churchfield, Lee, Moriarty, *et al*., 2012). The turbine rotor's modeling was simplified using the actuator line method, which represents the rotor's aerodynamics without considering the presence of the nacelle and tower. For meshing strategy, this work highlighted the importance of using local grid refinement to capture the meter-scale details of the turbine wake and the kilometer-scale turbulent atmospheric structures. Although the CFD-based approach can give comprehensive and accurate solutions, its usability is not practically feasible for the optimization purposes of a wind farm due to its long execution time and high computational resources (Shourangiz-Haghighi *et al*., 2020).

Another approach to address experimental and computational limitations is employing the analytical approach, best known for its practical yet accurate solution and computationally affordable (Göçmen *et al*., 2016). In general, the analytical approach uses the simplification of conservation of mass and momentum to predict the wake flowfield. However, detailed wake features such as instantaneous wake-center position at specific downstream distances are beyond its prediction capability due to some simplifications and assumptions during the derivation process of the equations. Nevertheless, this approach can give accurate predictions of the mean wake flowfield behind the HAWT, particularly within far-wake regions (Kaldellis *et al*., 2021), and multiple wakes behind HAWTs within wind farms by employing wake superposition models (Lanzilao & Meyers, 2022; Niayifar & Porté-Agel, 2016). In addition, the approach's ability to reasonably estimate wind farm power production in quick execution time makes it suitable for wind farm layout optimization (Archer *et al*., 2018). Hence, this work is intended to investigate the wake flow behavior behind the HAWT analytically.

The analytical approach for wake modeling has been extensively used over the past four decades by the wind energy industry, such as the pioneering industry standard Jensen wake model (Jensen, 1983; Katic *et al*., 1986). In this model, the wake was assumed to expand linearly as the downstream distance increased where its decay rate was controlled by the prescribed decay coefficient. The model used a top-hat approach where the averaging velocity deficit inside the wake cross-section was considered constant. This assumption could result in a large deviation in the downstream turbine power estimation since its power output is a function of the cube of the upstream velocity (Burton *et al*., 2011). Thus, the detailed prediction of the wake velocity profile becomes imperative for a wind farm power prediction.

During the past decade, several wake models have been developed with careful estimation of the wake velocity profile. A wake model developed by (Bastankhah & Porté-Agel, 2014) becomes a stepping stone to analytical wake modeling that considers the conservation of mass and momentum based on a single-Gaussian (SG) approach. The model showed its ability to accurately predict the velocity deficit under varying operational conditions of the HAWTs. However, this model has a major drawback regarding its incompatibility within the near-wake region, where the wake profile tends to follow a double-Gaussian (DG) shape (Krogstad & Eriksen, 2013; Magnusson, 1999).

The incompatibilities for the wake profile predictions within the near-fields were also found in the other analytical models (Frandsen *et al*., 2006; Ge *et al*., 2019; He *et al*., 2021; Ishihara & Qian, 2018; Xie & Archer, 2015), which used practical standpoints regarding their applications. As a result, those models are unable to properly estimate the wake evolution within the full region. However, a correct understanding of wake aerodynamics within a full-wake region becomes extremely important for HAWT micrositing. Hence, this work is dedicated to analytically predicting the HAWT wake aerodynamics within a full-wake region.

Some preceding works regarding analytical full-wake modeling have been reported in the literature. A foundation for analytical full-wake modeling considering the conservation of mass and momentum was introduced by (Keane *et al*., 2016), which was corrected by (Schreiber *et al*., 2020), and later revisited by (Keane, 2021) due to an issue in the derivation process of the model. This analytical approach, a double-Gaussian (DG) wake model, was proven experimentally and numerically to provide reliable predictions of wake distributions within a full-wake region. It was observed that two local minima around the blade midspan within the near-wake region gradually shifted towards the hub centerline due to effective turbulence mixing.

Further work complemented the developed DG model by considering the stability effects in terms of anisotropic wake expansion in lateral and vertical directions, thus facilitating its usability under different atmospheric thermal stability (Soesanto *et al*., 2022). Those developments in analytical full-wake modeling provide further insight into the wake transition mechanism behind the HAWT which covers both the near- and far-wake regions using a low-cost approach. Unfortunately, these DG-based models only apply to non-yawed HAWTs, where the direction of the prevailing wind velocity is aligned to the rotor axis. As a result, the models are unable to estimate the wake deflection downstream of the HAWT. Whereas, this prediction ability is necessarily needed in wake steering or wake control scenarios to minimize the shadow effects of the upstream HAWTs' wake experienced by the downstream HAWTs.

Several works have been conducted to develop the wake deflection models behind a yawed HAWT, where most of them were incorporated with the SG-based approach (Bastankhah & Porté-Agel, 2016; Lopez *et al*., 2019; Qian & Ishihara, 2018). Their predictions of wake distributions behind the yawed HAWT were accurate within the far-wake region. However, the effect of maximum lift around the blade midspan that generates the DG shape distribution within the near-wake region was unable to be reproduced correctly, emphasizing the importance of further development within this near region.

The novelty of this work is the development of the DG-based analytical wake model considering the conservation of mass and momentum for the wake velocity prediction under yaw misalignment. To the best of the authors' knowledge, this work is the first analytical wake model for the wake velocity prediction behind the yawed turbine that relied on the DG approach. This work extends the previous analytical works by incorporating the existing wake centerline deflection model with the DG-based approach to predict the streamwise velocity within a full-wake region behind HAWT under yaw misalignment. The results were validated against a high-fidelity LES dataset of the wake flowfields behind a HAWT under varying yaw configurations. The present study is expected to provide further insight into the wake evolution and its transition mechanism behind the yawed HAWT using low-cost analytical modeling. The methodology for the basic derivation of the model is presented in Section 2. Next, a brief description of LES case studies used in this work to validate the DG yaw wake model is drawn in Section 3. The results of the model's predictions and their statistical evaluations are presented in Section 4. Finally, a conclusion and a related future work are summarized in Section 5.

2. Methodology

2.1 The DG-based wake modeling considering yaw misalignment

Kinetic energy provided by the incoming wind is converted into mechanical energy by the HAWT rotor blades, causing momentum loss behind the HAWT. To maximize overall wind farm output, wake steering is found to be an effective strategy for suppressing power losses due to wakes (Vollmer *et al.*, 2016). One of which controls the yaw position of the upstream HAWTs to deflect their wakes, thus minimizing their negative impacts on the downstream HAWTs' performance. An illustration of the wake evolution behind a HAWT under yaw misalignment is shown in Figure 1.

The undisturbed incoming wind velocity U_∞ is extracted by the yawed HAWT to rotate its rotor. The wind energy exploitation causes a pressure drop between both sides of the rotor, creating a wake area behind the HAWT. The wake area evolving downstream of the HAWT has a specific recovery rate, which depends on the turbine's operating and ambient conditions. One of the notable characteristics of the wake is the velocity deficit ΔU within its area, which reduces the available wind energy for the downstream turbine.

In general, the wakefield can be categorized into two main regions, the near- and the far-wake regions. Within the near-wake region, the maximum velocity deficit or local minima is located around the blade midspan due to the maximum lift during the energy extraction process by the rotor (Magnusson, 1999). As a result, the mean velocity profile follows a DG distribution, as illustrated in Figure 1. In addition, an annular shear layer is produced due to the velocity difference between the near-wake and its ambient (NEL, 2014). As the downstream distance increases, momentum transfer due to turbulence mixing within the layer shifts two local minima laterally toward the wake center. This occurrence transforms the DG wake shape into the SG shape distribution, indicating the onset of the far-wake region. Meanwhile, the far-wake flowfield is less influenced by the detailed turbine features but more dominated by the ambient flow conditions and global-wind turbine parameters such as thrust coefficient C_T (Porté-Agel *et al.*, 2020).

The wake trajectory is strongly influenced by the rotor yaw angle (Doekemeijer *et al.*, 2020). In this matter, the rotor yaw angle controls the misaligned degree of the HAWT orientation against the prevailing wind direction. Here, the yaw rotor angle, γ, is defined as positive in the clockwise direction. In general, the yawed rotor causes the wake to deflect perpendicular to the prevailing wind direction. For a non-yawed condition, the mean wake trajectory is approximately perpendicular to the rotor plane.

From the analytical standpoint, the axial momentum balance resulting from the wind energy extraction process by an isolated HAWT can be approximated by one-dimensional momentum theory within the stream tube control volume (Sørensen, 2016). Considering the conservation of mass and momentum with some physical assumptions (Frandsen *et al.*, 2006), the axial momentum of the HAWT wake deriving from the stream tube approach can be expressed as follows:

$$T = \rho \int U_w (U_\infty - U_w) dA_w \quad (1)$$

where T is thrust force or total axial forces perpendicular to the rotor plane and exerted on the stream tube control volume, ρ is the air density, A_w is the wake cross-sectional area, U_∞ is undisturbed incoming velocity, and U_w is wake velocity in the prevailing wind direction.

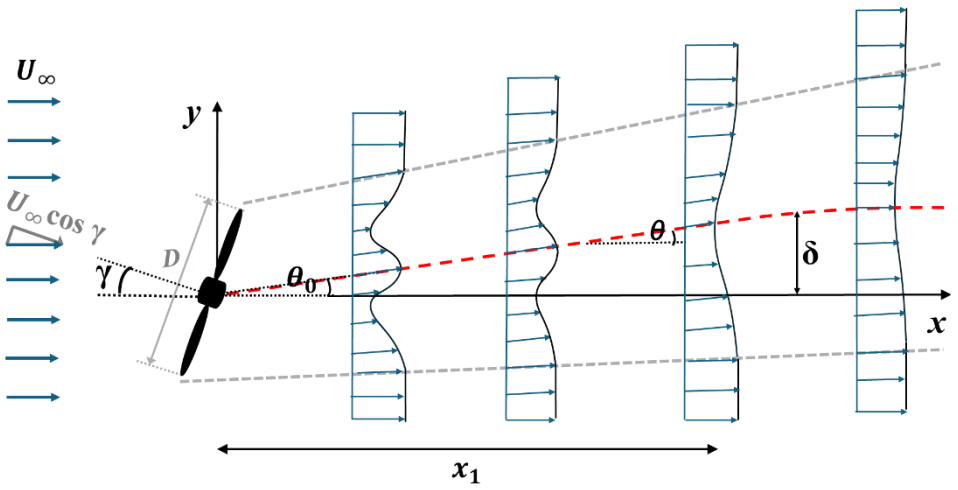

Fig. 1 An Illustration of hub-height wake evolution behind a yawed HAWT

In reality, the cross-sectional area of T acts perpendicular to the rotor disc plane is not precisely as the rotor disc area but an effective area A_e, thus allowing the velocity deficit to extend beyond the rotor area (Keane, 2021). However, the result of regression analysis R^2 showed very well fitness against lidar measurement data when the ratio of A_e/A=1. This means the effective area A_e empirically can be approximated as the rotor area A and is adopted in this study as a physical simplification. The thrust force T can also be expressed as a function of the thrust coefficient C_T using the following relation:

$$T = \frac{1}{2}\rho U_\infty^2 A C_T \tag{2}$$

To include the yaw misalignment, the thrust coefficient under the yaw condition $C_{T,y}$ is defined as follows:

$$C_{T,y} = \frac{T}{\frac{1}{2}\rho {U_{\infty,y}}^2 A} \tag{3}$$

where $U_{\infty,y}$ is the undisturbed incoming velocity perpendicular to the yawed rotor defined as follows:

$$U_{\infty,y} = U_\infty \cos\gamma \tag{4}$$

Considering the mass and momentum conservation, the streamwise wake flow field behind a yawed HAWT can approximated by equating Equations (1) and (3), resulting in:

$$\frac{1}{2}\rho\left(C_{T,y}\cos\gamma\right)^2 A\, U_\infty^2 \approx \rho \int U_w(U_\infty - U_w)dA_w \tag{5}$$

The wake velocity deficit behind a yawed HAWT as included in Equation 5, $\Delta U = U_\infty - U_w$, can be modeled as the product of velocity deficit amplitude $C(x)$ and wake spatial distribution $G(x,r)$ along the radial distance from the wake center r.

$$\Delta U = U_\infty[C(x)G(x,r)] \tag{6}$$

The relation in Equation 6 is of great importance to analytically model the normalized velocity deficit, which here is maintained to obey the conservation of mass and momentum. The momentum deficit downstream of the HAWT caused by wind energy extraction by the rotor can be modeled in the form of wake velocity U_w using the following relation:

$$U_w = U_\infty[1 - C(x)G(x)] \tag{7}$$

The wake velocity U_w gradually recovers as the downstream distance increases.

Considering the wake evolution within a full-wake region, the DG approach is used in this work to analytically predict the wake velocity distribution behind the yawed HAWT. The foundation for the analytical DG model applying the conservation of momentum was first established by (Keane *et al.*, 2016) and later by (Schreiber *et al.*, 2020). In this work, the existing amplitude function for the DG approach $C(x,\gamma)$, is modified to include the yaw misalignment effect using the following relation:

$$C(x,\gamma) = \frac{M - \sqrt{M^2 - \frac{1}{2}NC_{T,y}\cos\gamma\, D^2}}{2N} \tag{8}$$

where

$$M = 2\sigma_y\sigma_z \exp\left(\frac{-r_0^2}{2\sigma_y\sigma_z}\right) + \sqrt{2\pi} r_0 \sqrt{\sigma_y\sigma_z}\, \mathrm{erf}\left(\frac{r_0}{\sqrt{2}\sqrt{\sigma_y\sigma_z}}\right),$$

and

$$N = \sigma_y\sigma_z \exp\left(\frac{-r_0^2}{\sigma_y\sigma_z}\right) + \frac{\sqrt{\pi}}{2} r_0 \sqrt{\sigma_y\sigma_z}\, \mathrm{erf}\left(\frac{r_0}{\sqrt{\sigma_y\sigma_z}}\right).$$

r_0 denotes the radial position of the local minima, which here is set as a constant, r_0=0.26 (Soesanto *et al.*, 2022). Next, the radial distribution of the DG velocity deficit (Soesanto *et al.*, 2022) is modified here to include the wake deflection due to yaw misalignment:

$$G\big(r(y,z),\sigma(x)\big) = \frac{1}{2}\left(\exp\left[-\frac{1}{2}\left(\sqrt{\frac{(y-\delta)^2}{\sigma_y^2} + \frac{(z-z_h)^2}{\sigma_z^2}} + \frac{r_0}{\sigma}\right)^2\right] + \exp\left[-\frac{1}{2}\left(\sqrt{\frac{(y-\delta)^2}{\sigma_y^2} + \frac{(z-z_h)^2}{\sigma_z^2}} - \frac{r_0}{\sigma}\right)^2\right]\right) \tag{9}$$

where $\sigma = \sqrt{\sigma_y\sigma_z}$ is the geometric mean of wake expansion in the lateral direction σ_y and the vertical direction σ_z, which will defined later; δ is the wake center deflection due to yaw misalignment.

In this work, the SG-based wake deflection model developed by (Bastankhah & Porté-Agel, 2016) is incorporated with the present development of the DG yaw wake model. Thus, some relevant works by (Bastankhah & Porté-Agel, 2016) are adopted as follows:

$$\frac{\delta}{D} = \theta_0\frac{x_1}{D} + \frac{\theta_0}{14.7}\sqrt{\frac{\cos\gamma}{k_y k_z C_{T,y}}}\left(2.9 + 1.3\sqrt{1 - C_{T,y}} - C_{T,y}\right) \times \ln\left[\frac{\left(1.6 + \sqrt{C_{T,y}}\right)\left(1.6\sqrt{\frac{8\xi_y\xi_z}{D^2\cos\gamma}} - \sqrt{C_{T,y}}\right)}{\left(1.6 - \sqrt{C_{T,y}}\right)\left(1.6\sqrt{\frac{8\xi_y\xi_z}{D^2\cos\gamma}} + \sqrt{C_{T,y}}\right)}\right] \tag{10}$$

where

$$\xi_y = k_y\frac{(x - x_1)}{D} + \frac{\cos\gamma}{\sqrt{8}},$$

and

$$\xi_z = k_z\frac{(x - x_1)}{D} + \frac{1}{\sqrt{8}}.$$

k_y and k_z are wake growth constant in lateral and vertical directions, respectively. It should be noted that the lateral wake center deflection δ in Equation (11) applies for $x > x_1$. Otherwise ($x \le x_1$), the deflection formula $\frac{\delta}{D} = \theta_0\left(\frac{x}{D}\right)$, in which $\theta_0 \approx 0.3\gamma/\cos\gamma\left(1\sqrt{1 - C_{T,y}\cos\gamma}\right)$, is employed.

Here, the wake is assumed to evolve within the neutral atmospheric boundary layer (NABL) where the non-axisymmetric wake growth is quite small (Abkar & Porté-Agel, 2015). Hence, a single constant k^* could be used to represent

the wake growth rate in both lateral and vertical directions. The formulation is expressed as follows (Ishihara & Qian, 2018):

$$k^* = 0.11C_{T,y}^{1.07}TI^{0.2} \quad (11)$$

where TI is the hub-height inflow turbulence intensity in the streamwise direction.

It was observed from the experimental (Bastankhah & Porté-Agel, 2014) and numerical results (Abkar & Porté-Agel, 2015; Xie & Archer, 2015) that the wake tends to expand linearly under different inflow and turbine operating conditions. Therefore, the wake expansion function is modeled linearly here. As aforementioned regarding the similar wake growth constant k^* within the NABL, the asymmetry of wake expansion rates in the lateral and vertical directions is then strongly attributed to the yaw misalignment effect. A linear expansion function specifically derived for the DG wake model without tuning was derived by (Soesanto *et al.*, 2023), yet the application does not consider the yaw misalignment. To overcome this limitation, the linear DG expansion function in the lateral direction, where the yawed rotor has the most impact, is modified as follows:

$$\sigma_y = \frac{(0.1-0.2\sqrt{\beta}\cos\gamma+\varepsilon\cos\gamma)x}{x_1} + 0.2\sqrt{\beta}\cos\gamma - 0.1 \quad (12)$$

where the original β proposed by (Frandsen *et al.*, 2006) is modified to include the yaw misalignment:

$$\beta = \frac{1}{2}\frac{1+\sqrt{1-C_{T,y}}}{\sqrt{1-C_{T,y}}}$$

Meanwhile, the wake expansion in the vertical direction remains the same (Soesanto *et al.*, 2023):

$$\sigma_z = \frac{\left(0.1 - 0.2\sqrt{\beta} + \varepsilon\right)x}{x_1} + 0.2\sqrt{\beta} - 0.1 \quad (13)$$

where ε is initial wake expansion, located approximately at the far-wake onset, x_1. Using the formulation by (Schreiber *et al.*, 2020), the initial expansion ε is derived by enforcing the mass conservation between the Betz streamtube derived from the top-hat approximation (Frandsen *et al.*, 2006) and the DG approach.

$$\rho\frac{\pi}{8}D^2\beta\left(1-\sqrt{1-\frac{2}{\beta}C_T}\right) = \rho\pi M(\varepsilon)\frac{M(\varepsilon)-\sqrt{M(\varepsilon)^2-\frac{1}{2}N(\varepsilon)C_TD^2}}{2N(\varepsilon)} \quad (14)$$

Table 1
Benchmark case studies to validate the DG wake model considering yaw misalignment

Cases	γ (°)	U_{hub} (m/s)	TI (%)	$C_{T,y}$
Case 1	0	7.9	5	0.77
Case 2	10	7.9	5	0.80
Case 3	20	7.9	5	0.83
Case 4	30	7.9	5	0.89

It is worth noting that the value of ε needs to be solved numerically, one of which is by using a Matlab function *vpasolve* (Matlab, n.d.). Meanwhile, the length of the far-wake onset x_1 is approximated using the formula originally proposed by (Bastankhah & Porté-Agel, 2016), which was later modified by (Soesanto *et al.*, 2022) for the utility-scale HAWTs:

$$\frac{x_1}{D} = \frac{\cos\gamma\left(1+\sqrt{1-C_T}\right)}{\sqrt{2}c\left[4aTI + 2b\left(1-\sqrt{1-C_T}\right)\right]} \quad (15)$$

The coefficients a=0.58, b=0.077, and c=1.2.

The solution of amplitude function for the velocity deficit $C(x,\gamma)$ in Equation 9 applies if its discriminant, $V = M^2 - \frac{1}{2}NC_{T,y}\cos\gamma\, D^2$, is $V \geq 0$. Otherwise $(V < 0)$, an alternative physical solution derived from a mathematical standpoint is necessary. Following the same approach by (Keane, 2021), the following expression prevails for the velocity deficit amplitude under the yawed rotor, where $V < 0$:

$$C(x,\gamma) = \frac{\sqrt{M^2 + \left|M^2 - \frac{1}{2}NC_{T,y}\cos\gamma\, D^2\right|}}{2N} \quad (16)$$

2.2 Validation

The effectiveness of the DG yaw wake model was validated with the LES results of the wake flowfields behind the HAWT under varying yaw configurations. The benchmark dataset is a public database resulting from the numerical campaign of the European wind energy research project CL-Windcon, which can be useful for validation purposes (CENER, 2020). The LESs were conducted using a non-commercial solver SOWFA (Simulator fOr Wind Farm Applications) developed by the National Renewable Energy Laboratory (NREL) for wind farm simulations (Churchfield, Lee, & Moriarty, 2012). The solver has been verified to provide accurate prediction of wake flowfield and production of the real-world wind farm, such as Lillgrund windfarm in Sweden (Churchfield, Lee, Moriarty, *et al.*, 2012). There are four cases in total to evaluate the effectiveness of the DG yaw model, as further informed in Table 1.

A reference wind turbine developed by the Centre of Renewable Energy Sources and Saving (CRES), INNWIND 10 MW, with a diameter of 178.3 meters and a hub height of 119 meters (Chaviaropoulos *et al.*, 2013), was used in the simulation. The rotor was indirectly modeled by the actuator line model (ALM) (Sørensen & Shen, 2002), from which aerodynamic forces on the rotor are produced synthetically based on airfoil lookup tables, hence ensuring plausible wake aerodynamics behind the rotor. The SOWFA dataset of the 10-minute time-averaged wake flowfield at the hub height was used for validation.

The results between the benchmark dataset and analytical model were proportionally compared in the lateral and axial directions. The reference inflow velocity U_{hub} and turbulence intensity TI_{hub} in the prevailing wind direction were taken at the turbine hub height located 5D upstream of the turbine position to meet the undisturbed inflow condition. A total of 161 equally spaced measurement points in the lateral direction were placed within $-2 \leqslant y/D \leqslant 2$ with lateral spacing of $\Delta y/D$=0.025. Meanwhile, equally spaced measurement points were placed in the axial direction ranging within $1 \leqslant x/D \leqslant 12$. Those measurement locations were selected to cover a full-wake

region, allowing a comprehensive evaluation of the DG yaw wake model accordingly.

3. Results and discussion

3.1 Wake flowfield contours under varying yaw angles

Figure 2 shows the wake flowfield contours of the streamwise wake velocity at the hub height under varying yaw angles. Comparisons of the wake contours between the DG yaw model predictions and the benchmark SOWFA dataset are presented as a function of the normalized downstream distance behind the turbine x/D, and normalized lateral direction y/D. A valuable insight into the wake flowfield characteristics under varying yaw angles can be qualitatively observed and the degree of consistency between these two approaches is presented.

In general, the wake flowfield contours of all Cases 1-4 predicted by the DG yaw model agree well with the benchmark data. Under the aligned condition (Case 1, γ=0°), the wake centerline is maintained about the hub center (y=0) along the downstream distance. In addition, the wake is observed to expand linearly with the downstream distance. The velocity contours produced by both approaches confirm the lateral position of local minima that is located around the blade midspan, which evolves downstream up to $x/D \approx 3$. On the other hand, the velocity magnitude around the hub center position is higher than its surroundings, resulting in a DG velocity distribution within the near-wake region. Afterward, the two local minima shift toward the wake centerline and merge, producing an SG velocity distribution. At the farther downstream distance, the wake velocity gradually recovers to its undisturbed condition.

When the yaw condition is applied, the non-yawed wake trajectory shifts toward the lateral direction. In this case, a positive rotor yaw angle in the clockwise direction generates a lateral momentum, deflecting the wake to the positive lateral direction. Compared to the aligned condition, the rotor with γ=10° causes a relatively low wake deflection. The intensity heightens as the rotor yaw angle increases, which can be seen in Cases 3 (γ=20°) and 4 (γ=30°) from Figure 2. These results are reasonable since the projection of thrust force in the lateral direction F_y is directly proportional to the rotor yaw angle γ. Therefore, a higher γ results in a stronger lateral momentum to further deflect the wake trajectory from its aligned centerline.

One should keep in mind that the significance of wake deflection occurs mainly within the near-wake region, where the effect of turbine configuration such as rotor yaw angle γ has a strong contribution to the initial wake skew angle θ_0. This is confirmed by the benchmark and analytical results that show the wake trajectory deflection mainly occurred within the near-wake region. Afterward, the flow entrainment driven by shear turbulence is effectively mixed with the wake flowfield, attenuating the significance of the lateral momentum deflection within the far-wake region. As a result, only a trivial amount of lateral wake deflection remains within the far-wake region, represented by a small wake skew angle θ.

Both the numerical and analytical results consistently demonstrate the relationship between the wake recovery rate and the rotor yaw angle. It is confirmed that the proper yaw angle can effectively gain the wake recovery process, which will eventually improve the downstream turbine output. Specifically, the wake recovery increases with the yaw angle, as shown by the contour plots in Figure 2. This can be seen from the maximum velocity deficit area within the near-wake region that gradually fades out as the yaw angle γ increases. However, careful attempts should be made, especially regarding the blockage effects from the yawed HAWTs on the performances of their lateral neighboring HAWTs.

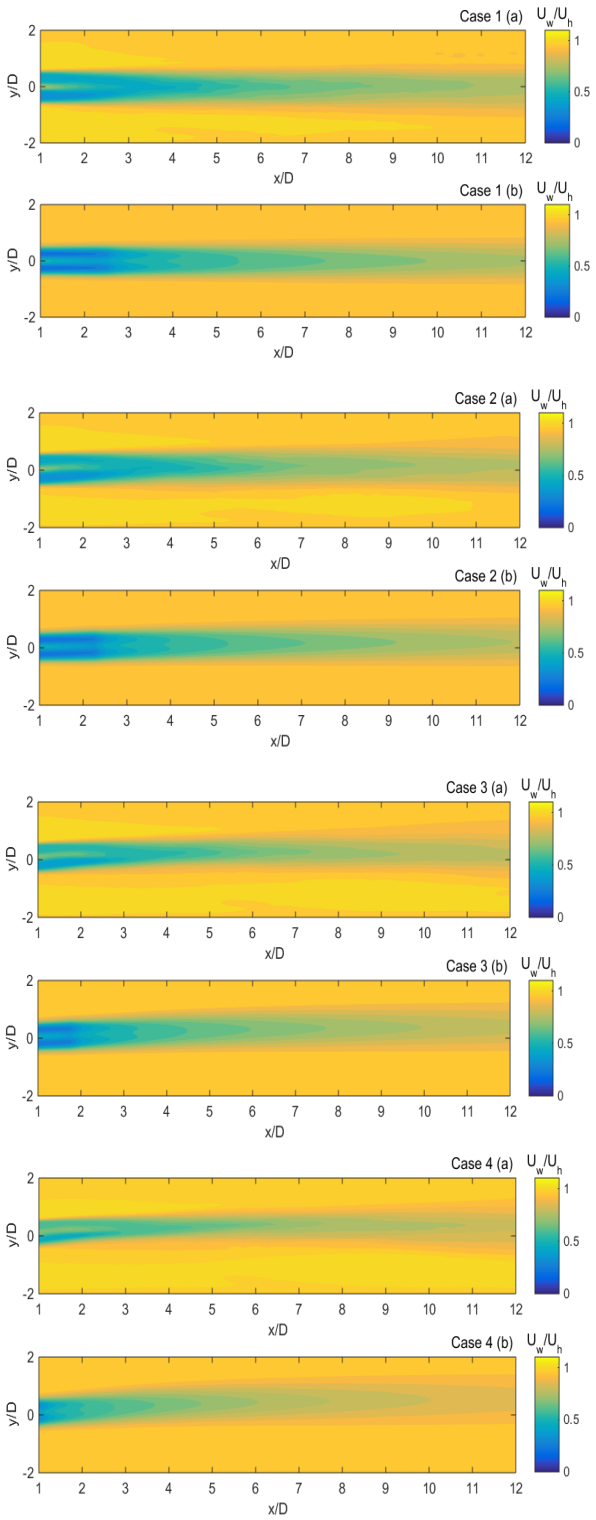

Fig. 2. Contours of wake velocity under varying yaw angles: (a) SOWFA (b) DG yaw wake model

3.2 Wake velocity profile under varying yaw angles

Further investigation of the wake characteristics under yaw misalignment was analyzed using hub-height wake velocity profiles in the lateral direction at several downstream distances behind the HAWT. Figure 3 shows the profiles of normalized wake velocity $\boldsymbol{U_w/U_h}$ under different yaw angles from Cases 1-4 estimated by the DG yaw wake model. The benchmark dataset resulting from SOWFA for the respective cases is also included for validation. The aligned position, which is located at y/D=0, is used as the reference for the wake center deflection. The benchmark data and wake model are equally compared at the same positions where the reference data were taken. There are 161 measurement points in total, spanning along the lateral direction ranging in $-2 \leqslant y/D \leqslant 2$ with an equal spacing of $\Delta y/D$=0.025. The profiles are sampled at 12 downstream positions behind the HAWT, located in $1 \leqslant x/D \leqslant 12$ with an equal spacing of $\Delta x/D$=1.

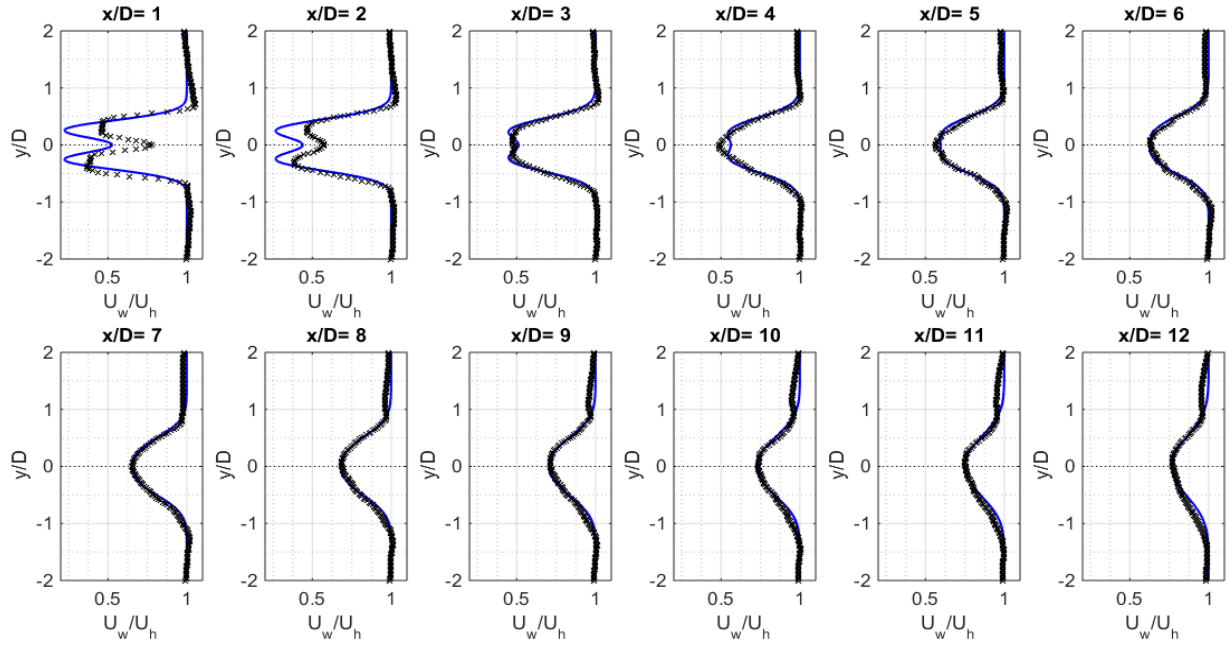

(c) γ=0°

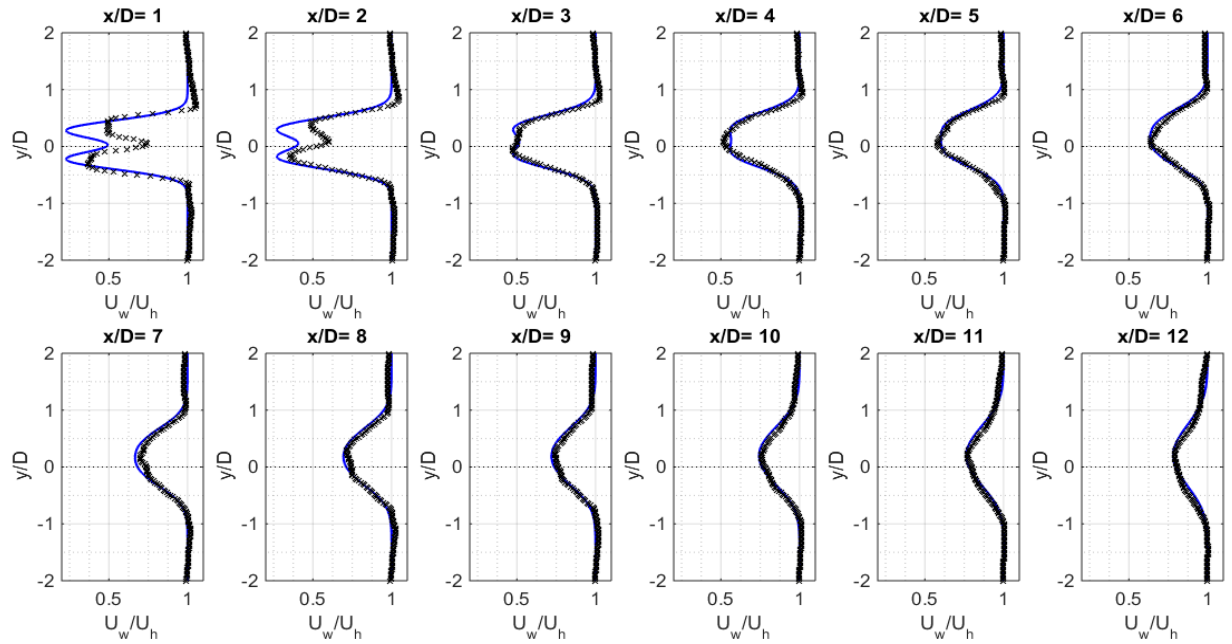

(d) γ=10°

Fig. 3 Profiles of normalized wake velocity U_w/U_h under varying yaw angles: ×SOWFA —DG yaw wake model

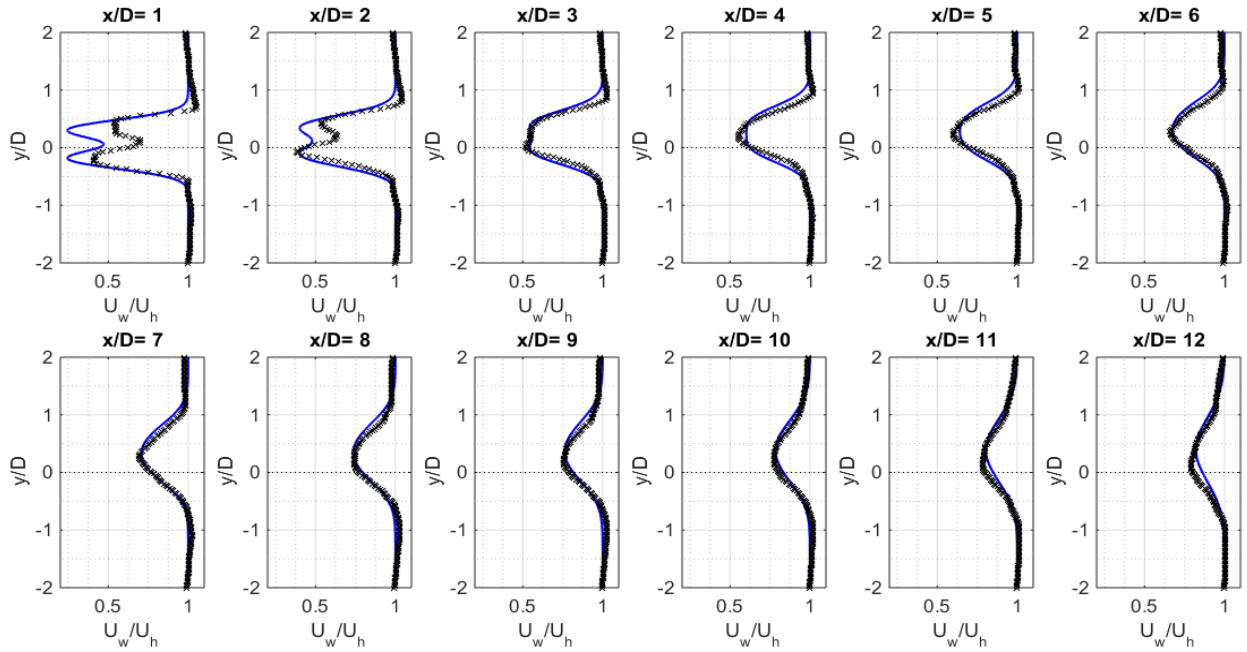

(a) γ=20°

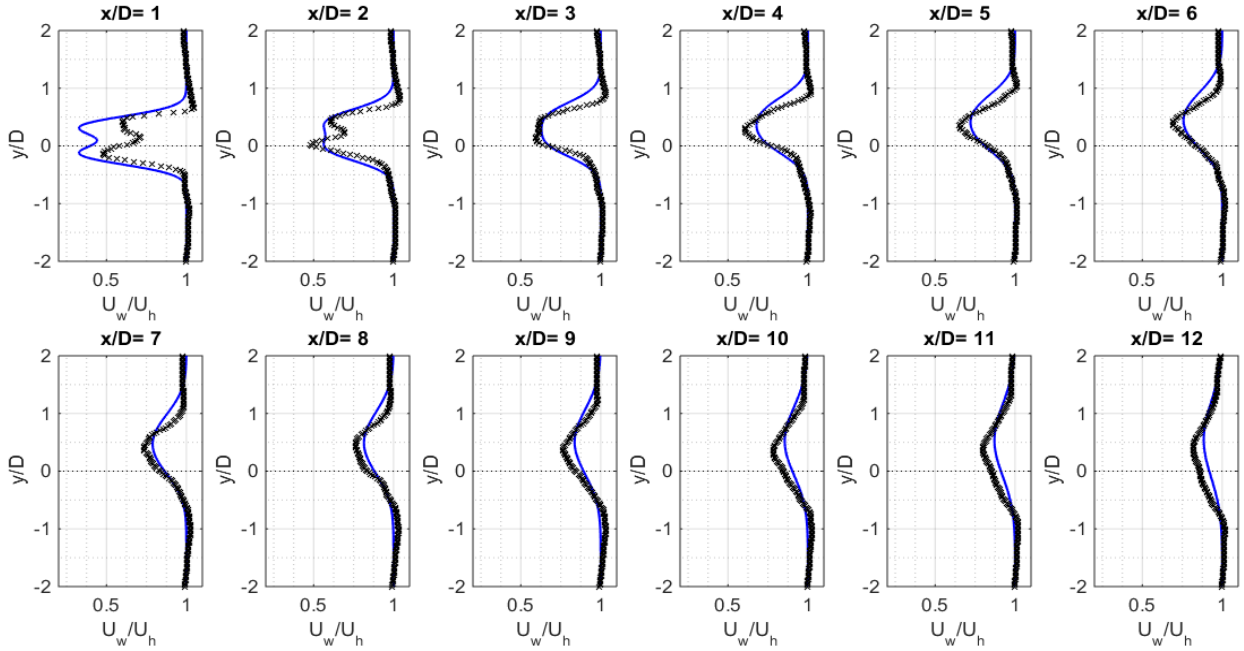

(b) γ=30°

Fig. 3 Profiles of normalized wake velocity U_w/U_h under varying yaw angles: ×SOWFA —DG yaw wake model **(Cont'd)**

At the non-yawed condition (γ=0°), the wake center trajectory along the evaluated downstream distances can be observed around the hub center. This position can cause a significant power loss on the aligned HAWT downstream due to wake shadowing. The wake deflection does not occur since the prevailing wind direction is perpendicular to the rotor, yielding a weak lateral force component that is not strong enough to steer the wake trajectory.

Within the near-wake region, the wake is found to form DG shape profiles. These formations happen due to the maximum lift generated around the blade midspan during the wind energy extraction by the HAWT rotor. Both numerical and analytical predictions show similar wake shape characteristics, where the two local minima represented by the maximum velocity deficit around the blade midspan generate the DG wake shape. Notable differences between the DG yaw wake model and the benchmark data under several yaw angles in Cases 1-4

can be observed clearly, mainly up to x/D=2. These discrepancies are inevitable due to the limitation of the DG yaw wake model that does not consider the wake acceleration effects owing to the turbine-induced wake turbulence.

In most Cases 1-4, the wake predictions by the DG yaw model have good agreement with the benchmark data. Conformable results among them are noticed starting from the onset of the far-wake region, about x/D=3, and remain in tune afterward. Around this far-wake onset, the wake velocity begins to transform from the DG to SG shape profile. This transformation is indicated by the lateral position of two local minima that shift towards the wake center. In addition, the significance of maximum velocity deficits at two local minima gradually diminishes as the downstream distance increases. At farther downstream distances, these two local minima merge and fully transform into the SG wake shapes, which in the evaluated cases start from $x/D\approx5$.

As re-emphasized in Figure 3, the wake deflection is strongly related to the yaw misalignment. Within the near-wake region, the lateral deflection of the wake trajectory linearly increases with the downstream distance, in contrast within the far-wake where the skew angle θ is small. Furthermore, both approaches demonstrate the effectiveness of yaw misalignment to control the wake recovery rate. Hence, the present investigation confirms the potential of rotor yaw control as a wake-steering strategy to improve overall wind farm production.

3.3 Wake recovery under varying yaw angles

The evolution of wake recovery under varying yaw angles can be analyzed using mean wake velocity $\overline{\boldsymbol{U}}_{\boldsymbol{w}}$ at the hub height along the downstream distances behind the turbine. Here, the root-mean-square was employed to statistically quantify the average value of wake velocity along the lateral direction. The measurement points equal to one rotor diameter spanning within $-0.5\leqslant y/D\leqslant0.5$ at the hub-height (z/D=0) with equal spacing of $\Delta\boldsymbol{y/D}$=0.025 were averaged to represent the wake velocity that potentially be exploited by the downstream turbine. In the streamwise direction, the data were sampled in the range of $1\leqslant x/\mathrm{D}\leqslant12$ with equal spacing of $\Delta\boldsymbol{x/D}$=0.25. To validate the reliability of the analytical model, the benchmark data from SOWFA at the same measurement points were also averaged and included for comparison.

The normalized mean velocity deficit $\Delta\overline{U}/U_h$ and mean wake velocity $\overline{U}_w/U_h$ resulting from the benchmark data and DG yaw wake model under varying yaw angles γ are presented in Figures 4 and 5, respectively.

In general, the predictions from the DG yaw model closely match the benchmark data, proving their eligibility to reasonably estimate $\Delta\overline{U}/U_h$ and $\overline{U}_w/U_h$ behind the HAWT under varying yaw angles. As shown in Figure 4, significant velocity deficit $\overline{U}_w/U_h$ is found up to $x/D\approx3$ behind the turbine, particularly for low yaw angles as in Case 1 ($\gamma=0^o$) and Case 2

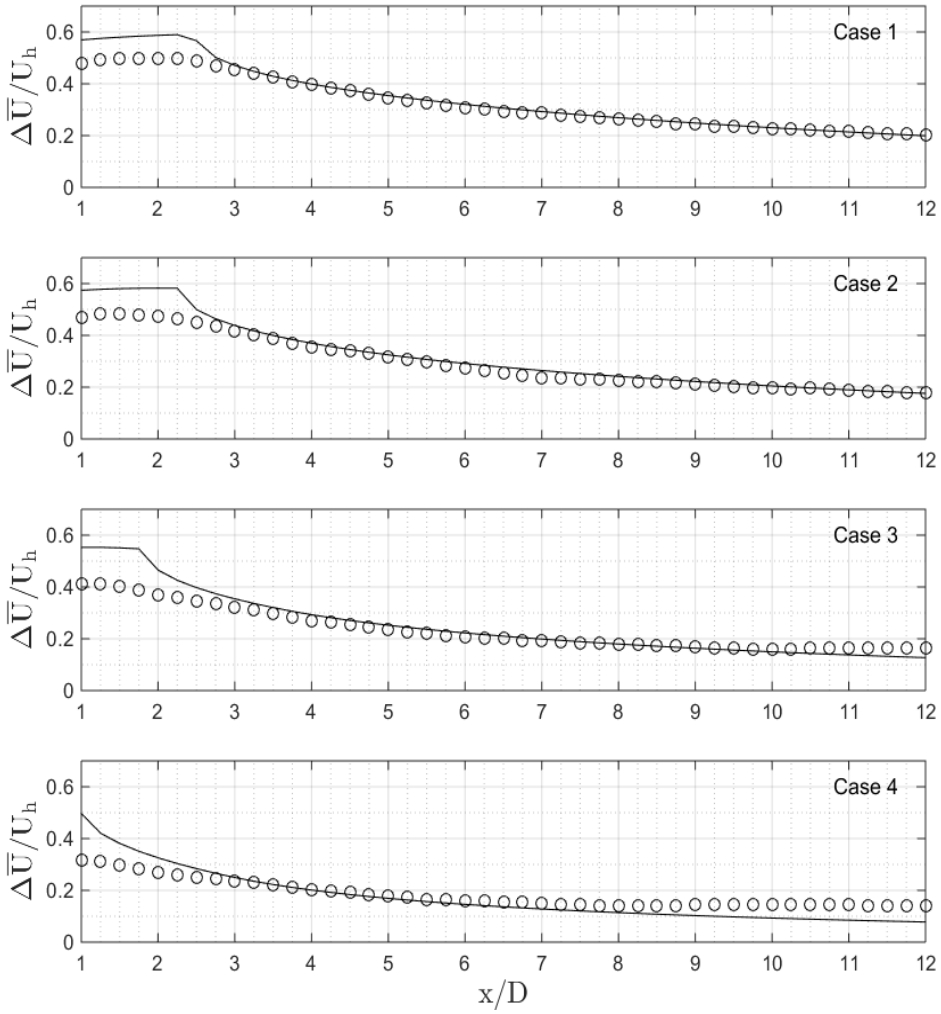

Fig. 4 The normalized mean velocity deficit $\Delta\overline{U}/U_h$ under varying yaw angles: O SOWFA —DG yaw wake model

(γ =10°). Meanwhile, its significance gradually reduces as the yaw angle increases, as in Case 3 (γ =20°) and Case 4 (γ =30°). It can be concluded that the predicted $\Delta\overline{U}/U_h$ under various yaw angles has a similar trend, where the region with a close distance of x/D from the turbine has the highest $\Delta\overline{U}/U_h$. Hence, this region should be avoided for turbine placement, particularly to minimize the aerodynamic losses due to wake interference from the upstream turbines.

In Figure 5, it can be observed that the wake recovery rate is strongly correlated to the rotor yaw angle. This correlation can be represented by the difference in mean wake velocity $\overline{U}_w/U_h$ at the same downstream distance x/D under varying rotor yaw angles. Specifically, a higher yaw angle gives a faster wake recovery. From all Cases 1-4, the wake decays exponentially, starting with a rapid recovery around the far-wake onset and gradually flattening at farther downstream distances. For offshore applications, the inter-row spacing between the turbines can be set as a "safe" zone, arranging the spacing distance as far as possible to minimize the wake loss effects. However, the same scenario cannot be applied to onshore applications, where territorial flexibility is tightly constrained. Thus, further work can be done to address the inter-row spacing problems to maximize wind energy capture.

From all Cases 1-4, salient discrepancies against the benchmark dataset are found to mainly occur within the near-wake region. In essence, the mean wake velocities from the benchmark data are higher compared to the analytical results. These discrepancies support the previous explanation where the neglect of the acceleration term in the governing equation to simplify the analytical DG modeling may lead to deviation. Particularly, within the near-wake region where the flow acceleration is likely to happen due to added turbulence intensity generated by the turbine. In addition, modest deviations can be observed in Case 4 (γ =30°) at approximately x/D≥9. These residuals may be attributed to wake meandering, which can disturb the flow stability within the far-wake region; thus affecting the accuracy of the analytical model that builds upon a fully developed flowfield approximation.

3.4 Available wind power within the wake region

The extracted kinetic energy from the flowing wind by the rotor causes a momentum loss behind the turbine. As a result, a significant loss of wind's aerodynamic power occurs within the wake region, particularly within the near-field. To analyze the overall power potential for electricity generation, the very first

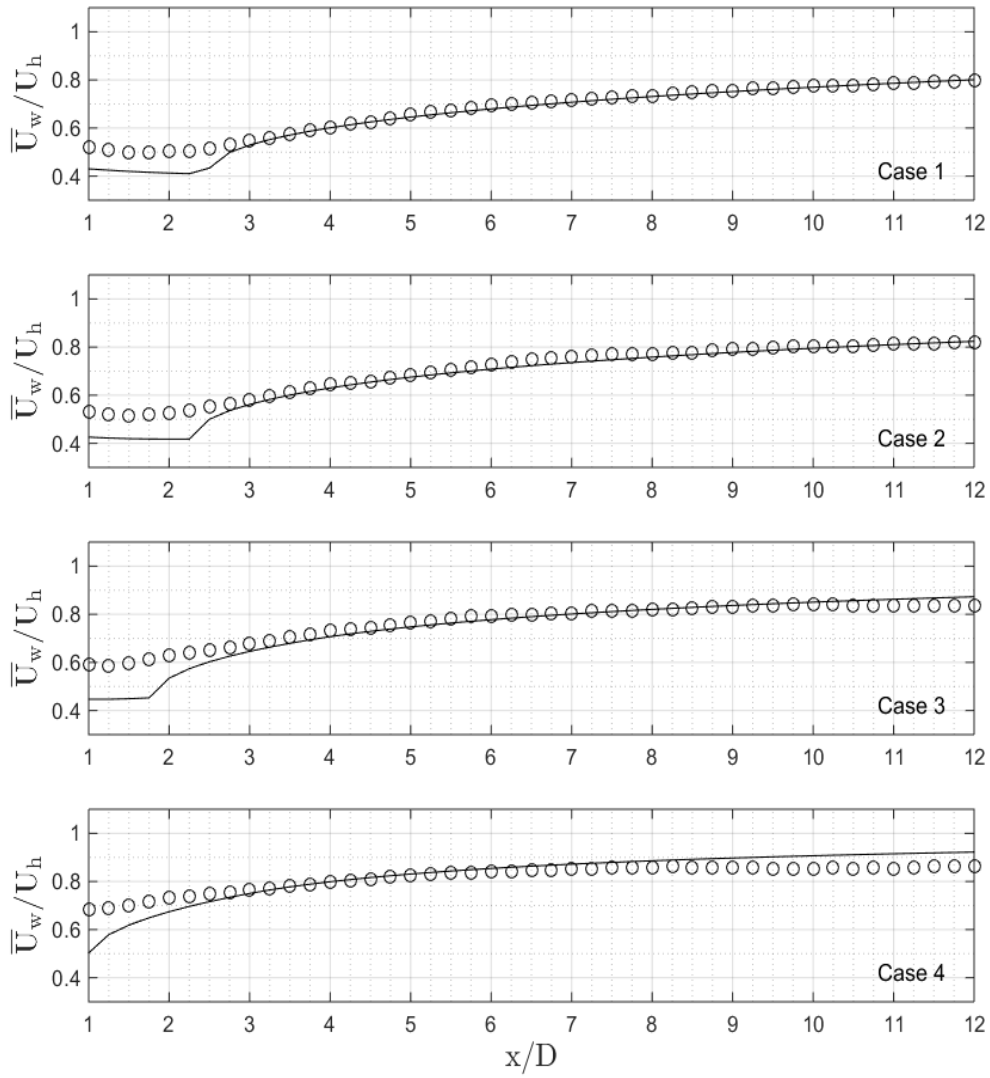

Fig. 5 The normalized mean wake velocity $\overline{U}_w/U_h$ under varying yaw angles: O SOWFA —DG yaw wake model

step that urges to be executed is estimating the available wind power within the wake region, P_w. In this study, the available wind power P_w is derived from the wake velocity U_w, where its magnitude is represented by the mean wake velocity $\bar{U}_w$ at the hub height.

$$P_w = \frac{1}{2}\rho A_0 \bar{U}_w^3 \quad (17)$$

where ρ is the air density and $A_0 = \pi D^2/4$ is the rotor swept area. In the case of inter-turbines, the downstream turbine output can be calculated by multiplying its power coefficient C_p with the incoming P_w from the upstream turbine. The effectiveness and efficiency of rotor yaw adjustment for the wind power enhancement are shown in Figures 6 and 7, respectively.

It is observed from Figure 6 that rotor yaw angle γ affects the amount of available wind power within the wake region. The power enhancement is directly proportional to γ. This yaw adjustment causes the wake to deflect away from its main trajectory, thus minimizing the aerodynamic loss due to wake shadowing. Compared to the baseline configuration (γ =0°), a higher γ is found to give a higher power improvement.

Figure 7 shows the power ratio P_w/P_f under the wake and freestream conditions. Equation 17 is also used to calculate the wind power under the freestream condition (P_f), where the undisturbed hub-height incoming velocity U_h of the respective cases substitutes the mean wake velocity $\bar{U}_w$ in the equation. This evaluation allows quantifying the effect of γ on the power efficiency, regardless of the power magnitude gained. As shown in Figure 7, the power efficiency increases with γ. In addition, the intensity of efficiency is found to increase with the higher γ. These results confirm the effectiveness of γ adjustment to improve the available wind power efficiency within the wake region.

3.5 *Statistical measures*

To quantitatively forecast the effectiveness of the DG yaw wake model, statistical measures from all Cases 1-4 were employed. The root mean square error, *RMSE*, was used to measure the deviation between these two approaches. In

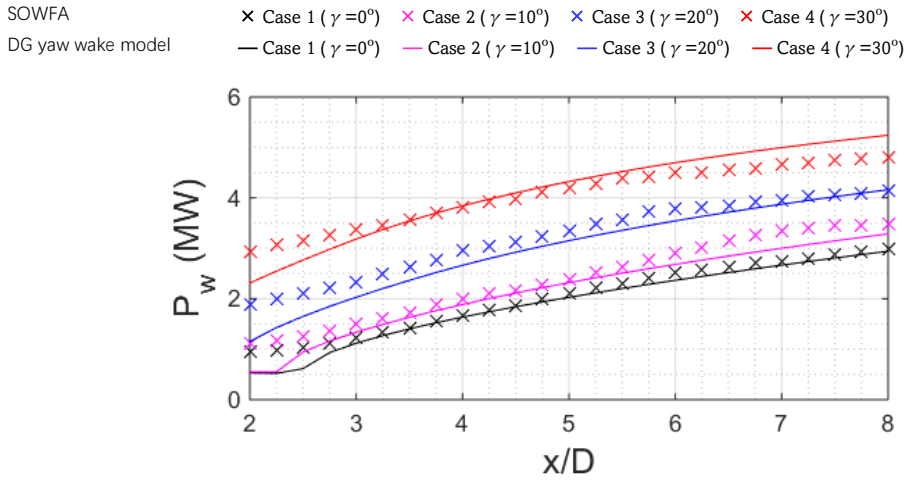

Fig. 6 The available wind power P_w within the wake region under varying yaw angles

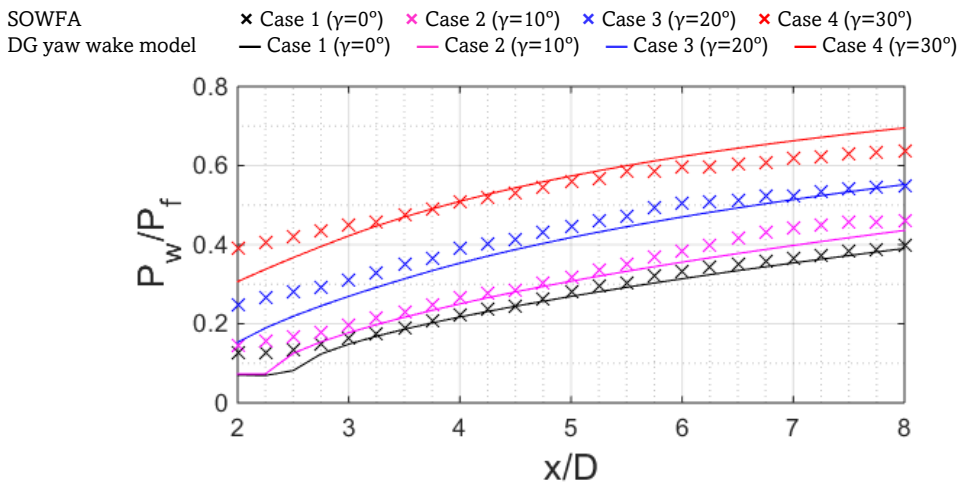

Fig. 7 The power ratio P_w/P_f under varying yaw angles

addition, the strength of linear dependence between the benchmark data and the model's results was measured using the Pearson correlation coefficient, R. Those statistical measures, which applied within $-2 \leqslant y/D \leqslant 2$ at each evaluated downstream distance $1 \leqslant x/D \leqslant 12$, are formulated as follows:

$$RMSE_{x/D} = \sqrt{\frac{\sum_{i=1}^{n}\left(U_{B,i} - U_{DG,i}\right)^2}{n}} \quad (18)$$

$$R_{x/D} = \frac{\left(U_{B,i} - \overline{U_B}\right) \times \left(U_{DG,i} - \overline{U_{DG}}\right)}{\sigma_B \times \sigma_{DG}} \quad (19)$$

where n is the total of measurement points in the y-direction; $U_{B,i}$ and $U_{DG,i}$ are the wake velocity from the benchmark data and analytical results at the i-th measurement point, respectively; $\boldsymbol{\sigma_B}$ and $\boldsymbol{\sigma_{DG}}$ refer to standard deviations of the benchmark and analytical data, respectively. The overbar $(\bar{\ })$ denotes the mean of the respective dataset. Perfect values for the *RMSE* and R would be 0 and 1, respectively.

Figure 8 shows the statistical results to evaluate the effectiveness of the DG yaw wake model. For all yaw angles in Cases 1-4, notable *RSMEs* occur particularly within the near-wake region. The highest *RMSE* of 0.11 can be found at x/D=1 for γ =30° (Case 4) and is remaining significant up to x/D=2. Afterward, the *RMSEs* values gradually decrease to approximately *RMSEs*≤0.05. Within the far-wake region, the model's deviations are relatively low, mostly less than 0.04 for all Cases 1-4. Meanwhile, *RMSE*s of Cases 1-4 are in the same range of *RMSEs*<0.03 at x/D≥6, except for Case 3 due to the wake meandering effect. These quantitative results demonstrate the model's reliability in predicting the wake velocity under varying yaw angles.

In general, linear dependence between the numerical and analytical results in all Cases 1-4 shows a strong positive correlation. This means that the wake shapes predicted by the DG yaw model are in tune with the benchmark data, allowing its usability to approximate the wake shape evolution within a full-wake region. Among the evaluated cases, the rotor yaw angle γ =30 ° (Case 4) has a lower association with the respective benchmark data. Yet, its linearity degree is still categorized as strong, indicated by the correlation coefficient of R>0.9 at each evaluated downstream distance. Meanwhile, the linear associations in the other cases are much higher, with a coefficient of R>0.96 in most of the downstream distances. The statistical measure results through *RMSE* and R emphasize the model's potential to predict effectively the wake shape distribution within a full-wake region under varying yaw angles.

4. Conclusion

The present study develops a DG-based analytical wake model considering the conservation of mass and momentum for the wake velocity prediction behind the yawed HAWT. The model extends the existing DG analytical wake model to include the yaw misalignment effect in the wake distribution behind an isolated yawed HAWT. The wake flowfields from several rotor yaw angles of 0°, 10°, 20°, and 30° were analytically modeled

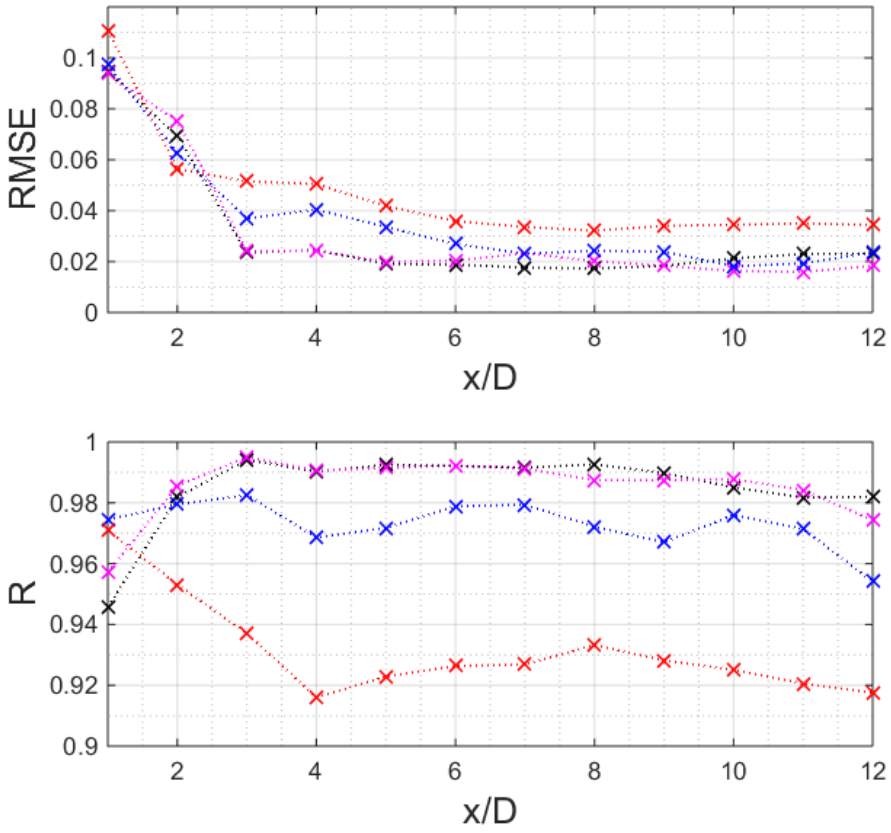

Fig. 8 Statistical measures of *RMSE* and R between SOWFA and DG yaw wake model under varying yaw angles: ×Case 1 ×Case 2 ×Case 3 ×Case 4

and analyzed. High-fidelity LES data resulting from SOWFA were used to validate the effectiveness of the DG yaw wake model. The wake flowfield contours under varying yaw configurations predicted by the analytical DG model agreed well with the benchmark data. It was observed that the yaw misalignment effectively deflected the wake trajectory, where its lateral displacement magnified as the yaw angle increased.

Further investigation of the rotor yaw effects on the wake profile distribution was also conducted using the DG yaw wake model, which was verified by the LES data. Both numerical and analytical approach results were consistent, though some deviations arose, particularly within the near-wake region. These deviations were further highlighted in the $\Delta\overline{U}/U_h$ and $\overline{U}_w/U_h$ comparisons between the two approaches, where the benchmark data produced lower $\Delta\overline{U}/U_h$ and higher $\overline{U}_w/U_h$ under all yaw configurations in Cases 1-4. The deviations were inevitable because the flow acceleration effect within the near-wake region, caused by turbine-induced turbulence, is not considered in the present model. In addition, the effectiveness and efficiency of rotor yaw adjustment for the wind power enhancement were evaluated. The results confirm the effectiveness of the rotor yaw adjustment in improving the available wind power efficiency within the wake region.

The effectiveness of the DG yaw model was quantitatively measured using statistical analyses through *RMSE* and Pearson correlation coefficient *R*. From the evaluated Cases 1-4, notable deviations were observed, particularly within the near-wake region due to the model's simplification that does not consider the acceleration effect by the turbine-induced turbulence. In contrast, the deviations were relatively small within the far-wake region, demonstrating the model's potential in estimating the wake velocity for micrositing. Meanwhile, strong positive correlations between the numerical and analytical results under varying yaw angles verify the model's ability to approximate the wake shape evolution within a full-wake region.

In general, the DG yaw model can provide valuable insight into a full-wake evolution behind an isolated HAWT under yaw misalignment. The present study asserts the importance of wake steering control by deflecting the wake trajectory away from the downstream HAWT to effectively enhance the wake recovery rate along the prevailing wind direction. Therefore, proper rotor yaw configuration can become a key to maximizing wind speed potential extracted by the downstream HAWT as a strategy to improve wind farm production. Future work could add the acceleration term in the DG yaw wake model derivation based on the conservation of mass and momentum. This may improve the model's accuracy within the near-wake region.

Acknowledgments

The authors express their gratitude to the CL-Windcon project team, who provided the SOWFA dataset for validation purposes, and acknowledge Badan Riset dan Inovasi Nasional (BRIN) and Universitas Diponegoro (UNDIP) for supporting this research project.

Funding: None.

Conflicts of Interest: The authors declare no conflict of interest.

References

Abkar, M., & Porté-Agel, F. (2015). Influence of atmospheric stability on wind-turbine wakes: A large-eddy simulation study. *Physics of Fluids*, *27*(3), 35104. https://doi.org/10.1063/1.4913695

Archer, C. L., Mirzaeisefat, S., & Lee, S. (2013). Quantifying the sensitivity of wind farm performance to array layout options using large-eddy simulation. *Geophysical Research Letters*, *40*(18), 4963–4970. https://doi.org/10.1002/grl.50911

Archer, C. L., Vasel-Be-Hagh, A., Yan, C., Wu, S., Pan, Y., Brodie, J. F., & Maguire, A. E. (2018). Review and evaluation of wake loss models for wind energy applications. *Applied Energy*, *226*, 1187–1207. https://doi.org/10.1016/j.apenergy.2018.05.085

Bastankhah, M., & Porté-Agel, F. (2014). A new analytical model for wind-turbine wakes. *Renewable Energy*, *70*, 116–123. https://doi.org/10.1016/j.renene.2014.01.002

Bastankhah, M., & Porté-Agel, F. (2016). Experimental and theoretical study of wind turbine wakes in yawed conditions. *Journal of Fluid Mechanics*, *806*, 506–541. https://doi.org/10.1017/jfm.2016.595

Burton, T., Jenkins, N., Sharpe, D., & Bossanyi, E. (2011). Wind Energy Handbook. In *Wiley*. https://doi.org/10.1002/9781119992714.ch6

Calaf, M., Meneveau, C., & Meyers, J. (2010). Large eddy simulation study of fully developed wind-turbine array boundary layers. *Physics of Fluids*, *22*(1), 15110. https://doi.org/10.1063/1.3291077

CENER. (2020). *Closed Loop Wind Farm Control (CL-Windcon) - Research data* (Issue 727477). http://www.clwindcon.eu/research-data/

Chaviaropoulos, P. K., Chortis, D., & Lekou, D. (2013). INNWIND. D1.2.1 – Definition of the Reference Wind Turbine–Analysis of Rotor Design Parameters. *INNWIND.EU*, *November 2012*, 1–30.

Cheng, W.-C., & Porté-Agel, F. (2018). A Simple Physically-Based Model for Wind-Turbine Wake Growth in a Turbulent Boundary Layer. *Boundary-Layer Meteorology*, *169*(1), 1–10. https://doi.org/10.1007/s10546-018-0366-2

Churchfield, M., Lee, S., & Moriarty, P. (2012). Overview of the Simulator for Offshore Wind Farm Application (SOWFA). *NREL*, 109. https://www.nrel.gov/wind/nwtc/sowfa.html

Churchfield, M., Lee, S., Moriarty, P., Martinez, L., Leonardi, S., Vijayakumar, G., & Brasseur, J. (2012). A Large-Eddy Simulation of Wind-Plant Aerodynamics. In *50th AIAA Aerospace Sciences Meeting including the New Horizons Forum and Aerospace Exposition*. American Institute of Aeronautics and Astronautics. https://doi.org/doi:10.2514/6.2012-537

Creech, A., Früh, W. G., & Maguire, A. E. (2015). Simulations of an Offshore Wind Farm Using Large-Eddy Simulation and a Torque-Controlled Actuator Disc Model. *Surveys in Geophysics* 36(3). https://doi.org/10.1007/s10712-015-9313-7

Doekemeijer, B. M., van der Hoek, D., & van Wingerden, J. W. (2020). Closed-loop model-based wind farm control using FLORIS under time-varying inflow conditions. *Renewable Energy*, *156*, 719–730. https://doi.org/10.1016/j.renene.2020.04.007

Evwind. (2021). *MingYang Smart Energy launches new 16 MW offshore wind turbine*. https://www.evwind.es/2021/08/20/mingyang-smart-energy-launches-new-offshore-wind-turbine/82067

Frandsen, S., Barthelmie, R., Pryor, S., Rathmann, O., Larsen, S., Højstrup, J., & Thøgersen, M. (2006). Analytical modelling of wind speed deficit in large offshore wind farms. *Wind Energy*, *9*, 39–53. https://doi.org/10.1002/we.189

Ge, M., Wu, Y., Liu, Y., & Li, Q. (2019). A two-dimensional model based on the expansion of physical wake boundary for wind-turbine wakes. *Applied Energy*, *233–234*, 975–984. https://doi.org/10.1016/j.apenergy.2018.10.110

Ghaisas, N. S., Archer, C. L., Xie, S., Wu, S., & Maguire, E. (2017). Evaluation of layout and atmospheric stability effects in wind farms using large-eddy simulation. *Wind Energy*, *20*(7). https://doi.org/10.1002/we.2091

Göçmen, T., Laan, P. Van Der, Réthoré, P. E., Diaz, A. P., Larsen, G. C., & Ott, S. (2016). Wind turbine wake models developed at the technical university of Denmark: A review. *Renewable and Sustainable Energy Reviews*, *60*, 752–769. https://doi.org/10.1016/j.rser.2016.01.113

He, R., Yang, H., Sun, H., & Gao, X. (2021). A novel three-dimensional wake model based on anisotropic Gaussian distribution for wind turbine wakes. *Applied Energy*, *296*(January). https://doi.org/10.1016/j.apenergy.2021.117059

Ishihara, T., & Qian, G. W. (2018). A new Gaussian-based analytical wake model for wind turbines considering ambient turbulence intensities and thrust coefficient effects. *Journal of Wind*

Engineering and Industrial Aerodynamics. https://doi.org/10.1016/j.jweia.2018.04.010

Jensen, N. O. (1983). *A note on wind generator interaction* . Risø National Laboratory .

Kaldellis, J. K., Triantafyllou, P., & Stinis, P. (2021). Critical evaluation of Wind Turbines' analytical wake models. *Renewable and Sustainable Energy Reviews*, *144*, 110991. https://doi.org/10.1016/j.rser.2021.110991

Katic, I., Hojstrup, J., & Jensen, N. O. (1986). A simple model for cluster efficiency. *European Wind Energy Association Conference and Exhibition*. https://orbit.dtu.dk/en/publications/a-simple-model-for-cluster-efficiency

Keane, A. (2021). Advancement of an analytical double-Gaussian full wind turbine wake model. *Renewable Energy*, *171*, 687–708. https://doi.org/10.1016/j.renene.2021.02.078

Keane, A., Aguirre, P. E. O., Ferchland, H., Clive, P., & Gallacher, D. (2016). An analytical model for a full wind turbine wake. *Journal of Physics: Conference Series*, *753*, 32039. https://doi.org/10.1088/1742-6596/753/3/032039

Krogstad, P.-Å., & Eriksen, P. E. (2013). "Blind test" calculations of the performance and wake development for a model wind turbine. *Renewable Energy*, *50*, 325–333. https://doi.org/10.1016/j.renene.2012.06.044

Lanzilao, L., & Meyers, J. (2022). A new wake-merging method for wind-farm power prediction in the presence of heterogeneous background velocity fields. *Wind Energy*, *25*(2), 237–259. https://doi.org/10.1002/we.2669

Lopez, D., Kuo, J., & Li, N. (2019). A novel wake model for yawed wind turbines. *Energy*, *178*, 158–167. https://doi.org/10.1016/J.ENERGY.2019.04.120

Magnusson, M. (1999). Near-wake behaviour of wind turbines. *Journal of Wind Engineering and Industrial Aerodynamics*, *80*(1), 147–167. https://doi.org/https://doi.org/10.1016/S0167-6105(98)00125-1

Matlab. (n.d.). *vpasolve*. MathWorks. https://www.mathworks.com/help/symbolic/sym.vpasolve.html

McTavish, S., Feszty, D., & Nitzsche, F. (2013). A study of the performance benefits of closely-spaced lateral wind farm configurations. *Renewable Energy*, *59*, 128–135. https://doi.org/10.1016/j.renene.2013.03.032

Meyers, J., & Meneveau, C. (2012). Optimal turbine spacing in fully developed wind farm boundary layers. *Wind Energy*, *15*(2), 305–317. https://doi.org/10.1002/we.469

NEL. (2014). *Characterisation of Downstream Flow from Large Wind Turbines*. 100.

Niayifar, A., & Porté-Agel, F. (2016). Analytical modeling of wind farms: A new approach for power prediction. *Energies*, *9*(9), 1–13. https://doi.org/10.3390/en9090741

Pinto, M. L., Franzini, G. R., & Simos, A. N. (2020). A CFD analysis of NREL's 5MW wind turbine in full and model scales. *Journal of Ocean Engineering and Marine Energy*, *6*(2). https://doi.org/10.1007/s40722-020-00162-y

Porté-Agel, F., Bastankhah, M., & Shamsoddin, S. (2020). Wind-Turbine and Wind-Farm Flows: A Review. *Boundary-Layer Meteorology*, *174*(1), 1–59. https://doi.org/10.1007/s10546-019-00473-0

Porté-Agel, F., Wu, Y.-T., & Chen, C.-H. (2013). A Numerical Study of the Effects of Wind Direction on Turbine Wakes and Power Losses in a Large Wind Farm. *Energies*, 6(10), 5297–5313. https://doi.org/10.3390/en6105297

Qian, G. W., & Ishihara, T. (2018). A new analytical wake model for yawed wind turbines. *Energies*, *11*(3). https://doi.org/10.3390/en11030665

Schreiber, J., Balbaa, A., & Bottasso, C. L. (2020). Brief communication: A double-Gaussian wake model. *Wind Energ. Sci.*, *5*(1), 237–244. https://doi.org/10.5194/wes-5-237-2020

Shourangiz-Haghighi, A., Haghnegahdar, M. A., Wang, L., Mussetta, M., Kolios, A., & Lander, M. (2020). State of the Art in the Optimisation of Wind Turbine Performance Using CFD. *Archives of Computational Methods in Engineering*, *27*(2), 413–431. https://doi.org/10.1007/s11831-019-09316-0

Soesanto, Q. M. B., Yoshinaga, T., & Iida, A. (2022). Anisotropic double-Gaussian analytical wake model for an isolated horizontal-axis wind turbine. *Energy Science & Engineering*, *10*(7), 2123–2145. https://doi.org/10.1002/ese3.1120

Soesanto, Q. M. B., Yoshinaga, T., & Iida, A. (2023). A linear wake expansion function for the double-Gaussian analytical wake model. *Energy Science & Engineering (in Press)*. https://doi.org/10.1002/ese3.1427

Sørensen, J. N. (2016). General Momentum Theory for Horizontal Axis Wind Turbines. In *Research Topics in Wind Energy* (Vol. 4). http://link.springer.com/10.1007/978-3-319-22114-4

Sørensen, J. N., & Shen, W. Z. (2002). Numerical modeling of wind turbine wakes. *Journal of Fluids Engineering, Transactions of the ASME*. https://doi.org/10.1115/1.1471361

Vollmer, L., Steinfeld, G., Heinemann, D., & Kühn, M. (2016). Estimating the ake deflection donstream of a ind turbine in different atmospheric stabilities: An les study. *Wind Energy Science*, *1*(2), 129–141. https://doi.org/10.5194/wes-1-129-2016

Wang, T., Cai, C., Wang, X., Wang, Z., Chen, Y., Song, J., Xu, J., Zhang, Y., & Li, Q. (2023). A new Gaussian analytical wake model validated by wind tunnel experiment and LiDAR field measurements under different turbulent flow. *Energy*, *271*, 127089. https://doi.org/10.1016/j.energy.2023.127089

Wu, Y. T., Lin, C. Y., & Chang, T. J. (2020). Effects of inflow turbulence intensity and turbine arrangements on the power generation efficiency of large wind farms. *Wind Energy*, *23*(7). https://doi.org/10.1002/we.2507

Xie, S., & Archer, C. (2015). Self-similarity and turbulence characteristics of wind turbine wakes via large-eddy simulation. *Wind Energy*, *18*(10), 1815–1838. https://doi.org/10.1002/we.1792

Yu-Ting, W., Chang-Yu, L., Chien-En, H., & Shao-Dong, L. (2019). Investigation of Multiblade Wind-Turbine Wakes in Turbulent Boundary Layer. *Journal of Energy Engineering*, *145*(6), 4019023. https://doi.org/10.1061/(ASCE)EY.1943-7897.0000625